Towards personalized medicine: Photoacoustic imaging enables companion diagnosis and targeted treatment of lung cancer

Melissa Y. Lucero and Jefferson Chan*

Department of Chemistry and Beckman Institute for Advanced Science and Technology, University of Illinois at Urbana-Champaign, Urbana, IL 61801, United States

Abstract

Companion diagnostics (CDx) represent a new frontier in personalized medicine that promises to improve treatment outcomes by matching therapies to patients. Currently, these tests are limited in scope and cannot report on real-time changes associated with disease progression and remediation. To address this, we have developed the first photoacoustic imaging-based CDx (PACDx) for the selective detection of elevated glutathione (GSH) in lung cancer. Since GSH is abundant in most cells, it was essential to tune the reactivity of the benzenesulfonyl-based trigger to distinguish between normal and pathological states. Moreover, we designed a matching prodrug, PARx, that utilizes the same mechanism to release both a chemotherapeutic (Gemcitabine) and a PA readout. We demonstrate that PARx can inhibit tumor growth while sparing all other tissue from off target toxicity in a A549 lung cancer xenograft model. We envision that this work will establish a new standard for personalized medicine by employing a unique imaging-based approach.

Introduction

The Centers for Disease Control and Prevention estimates that there will be over 1.8 million new cases of cancer in the United States in 2020. Despite recent breakthroughs in cancer treatment that include new FDA approved drugs and immunotherapy, over a third of these patients will not survive. Lung cancer is expected be responsible for the majority of these deaths.[1] Disease heterogeneity and interpatient variability are major contributors for the poor efficacy and safety of common treatment regimens. Indeed, it is not uncommon for physicians to rely almost entirely on a trial and error approach when making therapeutic decisions.[2] A new frontier in personalized medicine that aims to overcome this major challenge is the application of companion diagnostics (CDx).[3] A CDx is a test that can provide essential information for determining which patients may benefit from a particular drug by detecting biomarkers critical for drug

activation.[4] For instance, a CDx for Herceptin (an immunotherapy for breast cancer) can identify the presence and expression levels of the target receptor, HER2, in a patient's tumor. However, most FDA-approved CDx are limited to *in vitro* testing which cannot account for factors such as biochemical changes that occur as the disease progresses. In order to provide accurate, real-time information, it is crucial to develop new molecular imaging-based CDx for aberrant cancer properties. It is noteworthy that most imaging probes targeting cancer have been developed for optical-based methods (e.g., fluorescence) which can only image in the millimeter depth range due to scattering and attenuation of light.[5] Photoacoustic (PA) imaging, on the other hand, is a noninvasive modality that utilizes near-infrared (NIR) light to induce the generation of ultrasound. Because ultrasound scatters 10^3 times less than light in biological tissues, high resolution images (tens of microns) can be obtained in the centimeter range.[6] PA imaging has already been employed clinically for the detection of breast cancer,[7] thyroid cancer,[8] inflammatory arthritis,[9] and scleroderma[10] in label-free studies. Recently, our group[11,12] and others have expanded the scope of PA imaging through the development of acoustogenic probes. Select examples include imaging agents for the detection of metal ion dysregulation,[13-16] hypoxia,[17-20] proteases,[21,22] and signaling molecules such as nitric oxide[23,24] and hydrogen sulfide.[25] By leveraging our expertise in probe design and molecular imaging, we now report the development of the first PA imaging-based CDx (PACDx), as well as a matching Gemcitabine-based prodrug (PARx) that utilizes the same activation mechanism to target lung cancer in a murine model system.

Results

The design of PACDx features two main components: 1) a near-infrared dye[26] capable of generating a strong PA signal upon irradiation and 2) a benzenesulfonyl trigger for detecting glutathione (GSH) via nucleophilic aromatic substitution (S_NAr) chemistry (**Figure 1a**). As the most abundant biological thiol in the body, GSH is essential for maintaining redox homeostasis and detoxifying xenobiotics.[27] Consequently, aberrant changes in the cellular levels of GSH are correlated with a variety of pathologies such as cancer.[28] Among the various cancer types, non-small cell lung carcinoma has the largest change in GSH levels for both patient derived tissue samples (up to 4-fold)[29] and human cell lines (up to 7-fold),[30,31] relative to healthy tissue and non-cancerous cell lines, respectively. With this in mind, we chose to develop a CDx assay for

lung cancer based on the detection of GSH via PA imaging. This represents a significant and exciting challenge because existing GSH-responsive triggers based on disulfide exchange[32] and S_NAr[33] chemistry are generally too reactive to distinguish GSH levels in lesions versus healthy tissue, let alone different cancer types. For instance, installation of the 2,4-dinitrobenzenesulfonate trigger onto our PA platform afforded a probe that was fully activated with only 100 μM GSH (~10-fold less than physiological levels) (**Figure 1b**). For this reason, this probe could not distinguish GSH levels across several mammalian cell lines (**Figure S1**). We hypothesized that increasing the electron density on the benzenesulfonyl core could attenuate the S_NAr reaction with GSH and thus, afford a new trigger with the appropriate reactivity between 0.1 to 10 mM. To this end, we synthesized a panel of fourteen probes, from which two promising candidates were identified (**Figures S2-4**). Specifically, replacement of the 4-nitro group with a trifluoromethyl substituent (compound 3) decreased the reactivity towards low concentrations of GSH (100 μM, 1 h) (**Figure 1c**); however, it was still too reactive in the presence of physiological concentrations (1 mM GSH, 11.9-fold turn-on response after 1 h). This result indicates there would be significant false positives if the probe was taken up by healthy tissue. Reducing the reactivity further by substituting the 2-nitro moiety with a fluoro group resulted in highly optimized trigger (**Figure 1d**). Activation of the resulting probe, PACDx, under physiological conditions was completely attenuated. On the other hand, a dose-dependent signal increase up to 31.6-fold was observed when PACDx was incubated with 10 mM GSH for 1 h. Prior to activation, PACDx does not absorb strongly within the PA window (680 - 950 nm); however, treatment with GSH induces a bathochromic shift into the NIR region (λ_{max} = 690 nm) (**Figure 1e**). Irradiation at this wavelength yields the strongest PA response (**Figure 1f**). A dose-dependent PA signal enhancement (R^2 = 0.99) was observed when PACDx was treated with increasing concentrations of GSH (**Figure 1g** and **1h**). In contrast, when PACDx was incubated with biologically relevant concentrations of cysteine (200 μM) and homocysteine (100 μM) there was no notable reactivity which further demonstrates the exceptional selectivity exhibited by our probe (**Figure S5**).

Next, we turned our attention to evaluating the performance of PACDx in live cells using confocal microscopy. Of note, PACDx activation can be conveniently monitored in both PA and fluorescent modes due to its multimodal imaging capabilities. In addition to examining PACDx in A549 lung cancer cells, we also imaged U87 glioblastoma cells (a brain cancer cell line) and HEK 293 cells (a non-cancerous cell line)

which are expected to have low GSH levels. When A549 cells were incubated with PACDx, we observed a highly fluorescent cytosolic and mitochondrial staining pattern (**Figure 2a**). In contrast, when A549 cells were pretreated with *N*-ethylmaleimide (NEM), a reagent used to reduce the levels of intracellular thiols, the fluorescence signal was ~50% dimmer (**Figure 2b**). To confirm that the decrease in intensity was due to GSH depletion, we treated a third set of A549 cells with a non-responsive probe featuring an electron rich 4-methoxybenzensulfonyl trigger (Ctrl-PACDx, **Figure S6**). As anticipated, these cells were almost completely non-fluorescent (**Figure 2c**). For further validation of GSH detection, U87 cells were treated with PACDx where we observe a similar trend comparable to A549 cell imaging (**Figure S7**). Of note, probes featuring this trigger typically serve as substrates for glutathione S-transferase (GST), an abundant cytosolic enzyme that catalyzes the conjugation of GSH to electrophilic centers.[34,35] Since the expression of GST may vary in cancer, reactivity with this enzyme can confound imaging results. Interestingly, when A549 cells (and U87 cells for further validation) were pretreated with ethacrynic acid,[36] a potent reversible inhibitor of human GST, prior to staining with PACDx, no effect on probe activation was observed (**Figure S8**). This data suggests that the S_NAr reaction between GSH and the trigger is not dependent on GST enzymatic activity. For PACDx to function as an effective CDx, it is essential for it to be able to accurately differentiate the relative GSH levels in lung cancer cells compared to other cancer types, as well as healthy cells. To our delight, the intensity of PACDx in A549 cells was indeed the highest relative to U87 and HEK 293 cells (**Figure 2e**). However, it is important to note that the signal from the U87 cells were significantly lower than that of the HEK 293 cells. To account for possible variations in probe uptake and retention that may be responsible for this result, we incubated PACDx with cell lysates from each cell line and obtained results consistent with what was observed in intact cells (**Figure S9**). This suggests that the intracellular levels of GSH is highest in A549 cells and lowest in U87 cells. This was confirmed with the established Ellman's assay which allows for accurate quantification of GSH levels in cell lysates (**Figure 2f**).[37]

Having successfully developed PACDx for the selective detection of elevated GSH levels in lung cancer cells, we turned our attention to designing a prodrug invoking the same GSH-mediated chemistry. We rationalized it would be possible to append a chemotherapeutic to the PACDx core by strategically installing a hydroxymethyl handle ortho to the phenolic alcohol. Upon removal of the 2-fluoro-4-nitrobenzenesulfonyl trigger, the resultant phenolate intermediate can fragment via a 1,4-elimination pathway to release the drug

and the corresponding dye (HD-CH_2OH) for PA imaging (**Figure 3a**). We selected to append Gemcitabine, an FDA-approved drug, because it is commonly used to treat non-small cell lung cancer through the inhibition of DNA synthesis.[38,39] However, as with many chemotherapeutics, Gemcitabine indiscriminately targets any rapidly dividing cell in the body which results to adverse effects such as myelosuppression and liver toxicity.[40] Masking the primary alcohol with a variety of capping groups have led to the development of Gemcitabine-based prodrugs displaying attenuated cytotoxicity until they are activated.[41] Although we could have directly modified Gemcitabine with our new 2-fluoro-4-nitrobenzenesulfonyl trigger, we wanted to leverage the PA imaging capabilities of the resulting prodrug (herein named PARx) to monitor drug release in real-time. PARx was synthesized starting from the sequential reduction of 2,4-dihydroxybenzaldehyde and TBS protection to afford **16** in 61% yield. *In situ* deprotection of the phenolic alcohols with sodium hydride facilitated a nucleophilic substitution and retro-Knoevenagel sequence with Cy7-Cl to obtain **17**. The GSH-responsive trigger was installed, and the primary alcohol was deprotected under acidic conditions to yield **18** (Ctrl-PARx-2) in 46% over 2-steps. Finally, a chloroformate intermediate was generated using phosgene which was reacted with Gemcitabine to obtain PARx (Supporting information).

With PARx in hand, we first evaluated whether attaching Gemcitabine would alter the PA imaging properties of the dye scaffold, as well as the responsiveness of the trigger to GSH. The wavelength of maximum absorption (λ_{max} = 700 nm) of HD-CH_2OH was red-shifted by ~10 nm relative to **1** (**Figure 1e** and **3b**). However, the wavelength associated with the strongest PA signal (690 nm) was identical for both dyes (**Figure 1f** and **3c**). We observed that irradiation of PARx consistently yielded a more intense PA signal, presumably due to the larger PA brightness value ($\varepsilon \times (1- \Phi_{Fl})$).[20] Importantly, the response to GSH was not affected as PARx could also be activated in a dose-dependent fashion (**Figures 3d** and **S10**). We also demonstrated that PARx displayed exceptional selectivity against a panel of metal ions, amino acids, reductants, reactive nitrogen species, reactive oxygen species, metabolic liver enzymes, and competing thiols (**Figure 3e**). Next, we employed MS and NMR analyses to confirm that GSH mediates the release of Gemcitabine (**Figures S11** and **S12**). To further support these results, we prepared a control compound (Ctrl-PARx-1) that is equipped with an unreactive 4-methoxybenzenesulfonyl trigger (**Figure S13**). MS analysis reveals that both the trigger and carbonate linkage of Ctrl-PARX-1 were stable in the presence of

10 mM GSH for at least 1 h (**Figure S14**). Moreover, when subjected to live cells, PARx could readily distinguish GSH levels in A549, U87, and HEK293 cells (**Figures 3f and S15**). Lastly, we assessed the cytotoxicity of PARx in A549 cells using the MTT assay. Our results indicate that PARx exhibits dose-dependent toxicity that is comparable to free Gemcitabine. On the contrary, when we treated cells with either Ctrl-PARx-1 or Ctrl-PARx-2, a second control reagent lacking Gemcitabine, the cytotoxicity was significantly attenuated (**Figure 3g**). Repeating the corresponding MTT assays in U87 cells clearly establishes that PARx requires the elevated levels of GSH found in A549 cells to effectively mediate the release of Gemcitabine.

To evaluate the *in vivo* efficacy of the PACDx and PARx pair, we established a A549 xenograft model of lung cancer. After the tumors had grown to a volume of ~100 mm^3 we administered PACDx via intratumor injection. Irradiation at 680 nm (the optimal in vivo wavelength) at the 1 h time point resulted in an increase in the PA signal by ~1.5-fold relative to the control flank which does not bare a tumor. These results are consistent with our *in vitro* findings and clearly demonstrate that our trigger can distinguish normal and pathological levels of GSH in live animals. Next, we introduced PARx via systemic administration (i.e., retroorbital injection) to determine its biodistribution profile, as well as potential off-target cytotoxic effects. We harvested tissue from vital organs 1 h post-injection for PA imaging analysis. The PA signals from the heart, kidneys, liver and spleen were not statistically different between the treatment and control groups (**Figure 4a** and **4b**). In contrast, the PA intensity of the tumor tissue was 1.2-fold higher for the PARx treated animals suggesting that activation and subsequent release of Gemcitabine was selective in tumors. The results from our PA imaging experiments suggest PARx will not have off-target toxicity. To asses this, we performed histological staining which revealed that there was minimal toxicity to the heart, kidneys, liver, and spleen in PARx treated animals (**Figure 4c**). However, PARx was highly toxic in tumor tissue as indicated by the decrease in the number of nuclei and size of the tumor cells. In addition, TUNEL staining revealed that the poor morphology observed was due to apoptosis induced by the release of Gemcitabine from PARx (**Figure 4d**).

Encouraged by these promising results, we set forth to determine whether PARx could function as an effective prodrug for the selective, GSH-mediated killing of lung cancer cells. Over a 21-day period, PARx

was administered to A549 xenografts via intratumoral injection every 7 days. PA imaging was performed 1 h after treatment to monitor Gemcitabine release (**Figure S16**). Compared to control tumors (**Figure 5a** and **5d)**, the PA signal was higher in PARx-treated tumors which indicates turnover of the 2-fluoro-4-nitrobenzenesulfonyl trigger (Figure **5b** and **5d**). Owing to the release of Gemcitabine, tumor growth was fully attenuated when treated with PARx (**Figure 5e**). On the contrary, tumors grew up to ~600 mm^3 in size (6-fold increase) when animals received a saline vehicle control. To evaluate the systemic compatibility of PARx, we retro-orbitally administered PARx every 7 days over the course of a 21-day period (**Figures 5e**). The inhibition of tumor growth using this dosing regimen was nearly identical to the results obtained via intratumoral administration. During the same time period, we monitored the animal's body weight as a measure of general toxicity over the course of treatment. Under no treatment conditions did we observe any loss of weight (**Figure 5f**) or change in behavior.[42] To further challenge the prodrug approach, we increased the dosing frequency of PARx from once every 7 days to once every 3 days (**Figure S17**). We hypothesized that we would not see any adverse effects, especially in the liver where severe damage is common with free Gemcitabine. Gratifyingly, we did not observe a change in the body weight (**Figure S18**) or behavior of the animals, nor did we detect any damage to the liver of the treated animals.

Discussion

The identification of disease biomarkers and the subsequent use of this information to guide therapeutic decision-making is a hallmark of personalized medicine. In this study, we have developed the first PA imaging-based CDx for the detection of GSH in lung cancer. A major advantage of employing an imaging-based approach rather than a conventional *in vitro* testing strategy, is the unique ability to visualize changes that occur during disease progression in real time. It is noteworthy that GSH is typically not considered to be an ideal cancer biomarker, even though it is elevated by up to 7-fold in lung cancer, because current sensing strategies are too insensitive to distinguish between normal and pathological levels, especially *in vivo* . For instance, we demonstrate that when the common 2,4-dinitrobenzenesulfonyl trigger is installed onto our PA platform, the resulting probe is fully activated within minutes with as little as 100 μM GSH. This proves difficult for use in living systems (e.g., live cells and animals) where GSH is present in all tissue at high concentrations (> 1 mM). By rationally modulating the structure and electronics

of the benzenesulfonyl trigger we have fine-tuned the S_NAr reactivity enabling us to develop PACDx which can reliably differentiate GSH in the 0.1 to 10 mM concentration range. Although several fluorescent probes have been developed using an analogous approach, they detect GSH indirectly via GST activity.[43] In contrast, we demonstrate PACDx is directly sensing GSH since inhibition GST had no effect on probe activation, presumably because PACDx is not a viable substrate for GST. This eliminates a potentially confounding variable since GST expression can vary across cancer types and is known to change throughout tumor progression.

In this study we also developed a highly effective prodrug (PARx) that utilizes the same GSH-mediated activation mechanism to selectively release Gemcitabine from a PA imaging dye. Although we could have directly installed the new trigger onto Gemcitabine, the ability to perform PA imaging provides us with a powerful handle to monitor and confirm drug delivery. We envision further exploiting this robust design since other drugs, as well as biologically relevant analytes can be appended for targeted delivery. With regards to Gemcitabine, it is an FDA-approved drug and one of the first line treatment options for various cancers including lung cancer. Unfortunately, it is characterized by rapid metabolism, poor bioavailability and low tumor uptake. As a result, frequent doses must be administered to ensure a therapeutic response. However, high levels of this drug result in adverse effects such as myelosuppression and severe liver damage. Since, PARx is only activated in lung cancer cells we were able to demonstrate through different dosing regimens (every 7 days versus every 3 days for 21 days) that PARx did not display any off-target toxicity. For instance, histological analysis of tissue samples harvested after the final dosing was identical to the non-treated control tissue. Lastly, PARx does not damage the liver because it is not processed by liver enzymes, as demonstrated by an in vitro assay where it was incubated with RLMs that contain a variety of cytochrome P450 enzymes.

In conclusion, this study showcases the potential use of PA imaging-based CDx to detect critical biomarkers for effective personalized therapy. In current studies we are employing PACDx and PA imaging to stratify animals based on GSH levels. This will allow us to predict, prior to treatment, which group of animals will have the greatest therapeutic efficacy when treated with PARx. On another important note, PA monitoring of drug release may also aid in the drug development process since confirmation of drug delivery in real-time is a major challenge. However, in the case of PARx, our in vitro assays demonstrate that the intensity

of the PA response correlates with the amount of drug being released. We envision that this work will establish a new standard for co-developed PA imaging-based CDx and safe prodrugs that both employ the same selective activation mechanism.

Acknowledgements

This work was supported the National Institutes of Health (R35GM133581). M.Y.L acknowledges the Alfred P. Sloan Foundation for financial support. Major funding for the 500 MHz Bruker CryoProbeTM was provided by the Roy J. Carver Charitable Trust (Muscatine, Iowa; Grant No. 15-4521) to the School of Chemical Sciences NMR Lab. The Q-Tof Ultima mass spectrometer was purchased in part with a grant from the National Science Foundation, Division of Biological Infrastructure (DBI-0100085). We also acknowledge the Core Facilities at the Carl R. Woese Institute for Genomic Biology for access to the Zeiss LSM 700 confocal microscope and corresponding software. M.Y.L. thanks Ms. Hailey Knox for initial animal training and assistance with the NanoZoomer. We thank Mr. Thomas Bearrood and Ms. Chelsea Anorma for assistance with initial confocal imaging experiments, Mr. Lucas Akin for aid with mass spectrometry experiments, and Prof. Sayeepriyadarshini Anakk and Ms. Angela Dean for help with interpreting results from H&E staining experiments.

Author contributions

M.Y.L. performed all experiments in this study that include chemical synthesis, *in vitro* characterization, cellular studies, tumor model studies, *in vivo* imaging, and sample preparation for *ex vivo* analysis. M.Y.L. and J.C. analyzed the data and prepared the manuscript. J.C. conceived the project with intellectual contributions from M.Y.L.

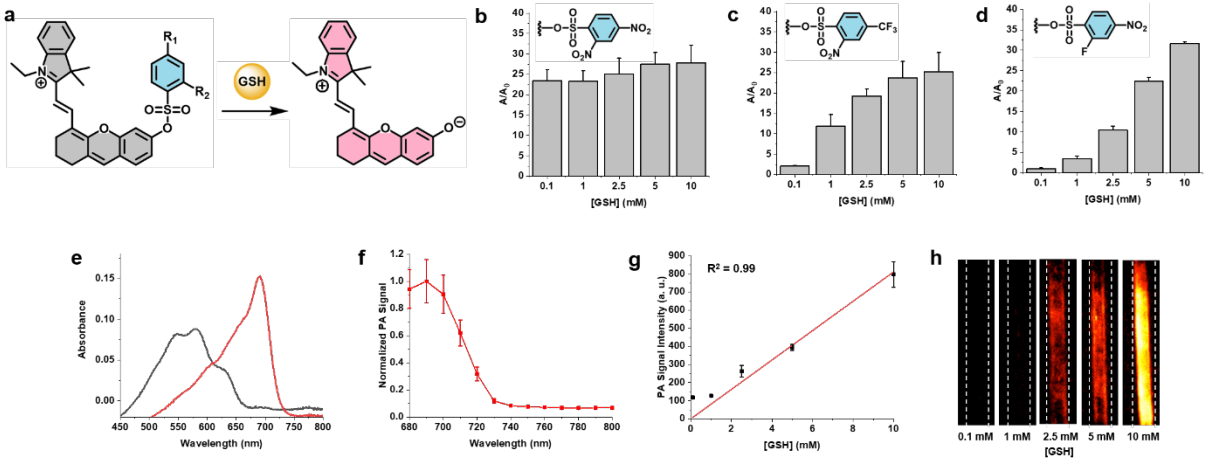

Figure 1. a) General schematic for GSH-responsive photoacoustic companion diagnostics. Dose-dependent activation of b) 2,4-dinitrobenzenesulfonyl HD, c) 4-trifluoromethyl-2-nitrobenzenesulfonyl HD; and d) 2-fluoro-4-nitrobenzenesulfonyl HD (PACDx) where [GSH] = 0.1 – 10 mM. Error bars = SD (*n* = 3). e) Absorbance profile of 5 μM PACDx before (black line) and after (red line) treatment with 10 mM GSH at 37 °C for 1 h (pH 7.4, 70% PBS/MeCN). f) PA spectra of 50 μM turned over HD dye in 70% PBS/MeCN. g) PA signal (*n* = 3) and h) PA images of PACDx (50 μM, 70 % PBS/MeCN, pH 7.4, 37 °C for 1 h) in response to GSH.

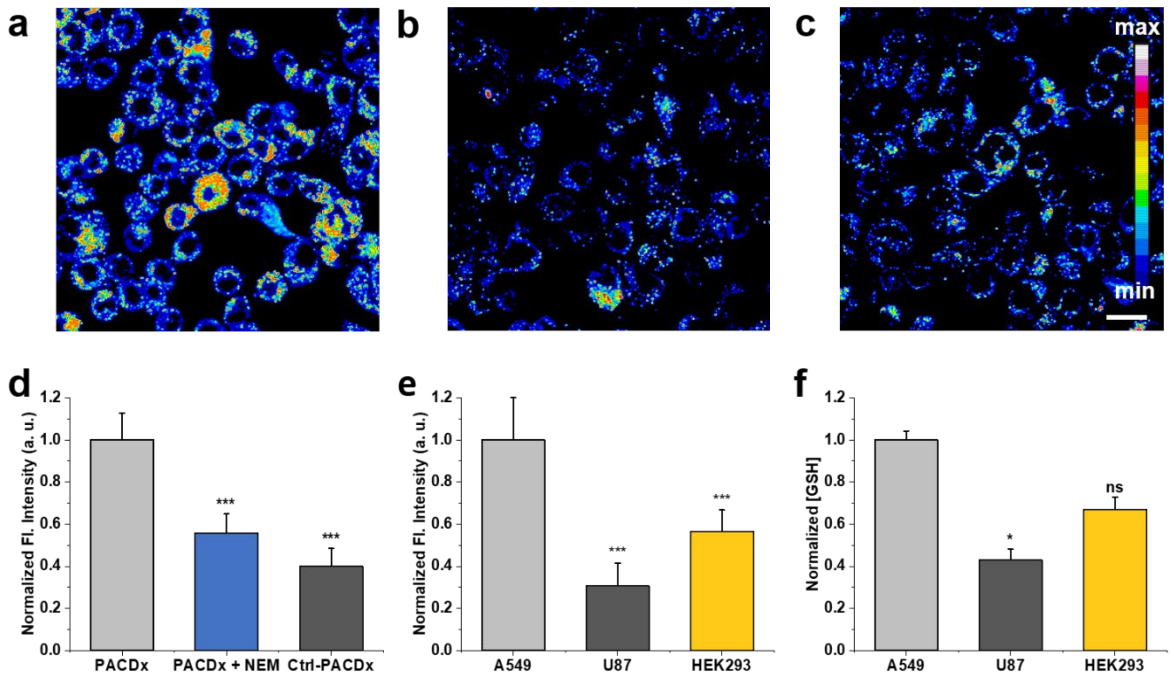

Figure 2. Confocal microscopy image representing a) A549 cells treated with 5 μM PACDx for 1 h at 37 ºC, b) A549 cells pre-treated with 1 mM NEM then incubated with 5 μM PACDx for 1 h at 37 ºC, and c) A549 cells treated with 5 μM Ctrl-PACDx for 1 h at 37 ºC. Scale bar represents 20 μm. d) Normalized fluorescence intensity obtained from cell imaging under conditions represented in a-c. Error bars = SD (n ≥ 3). e) Normalized fluorescence intensity obtained from cell imaging A549, U87, and HEK293 cells with 5 μM PACDx for 1 h at 37 ºC. Error bars = SD (n ≥ 3). f) Normalized [GSH] obtained from Ellman's assay. Error bars = SD (*n* = 2). Statistical analysis was performed using Student's t-test, ***: $p < 0.001$, relative to A549.

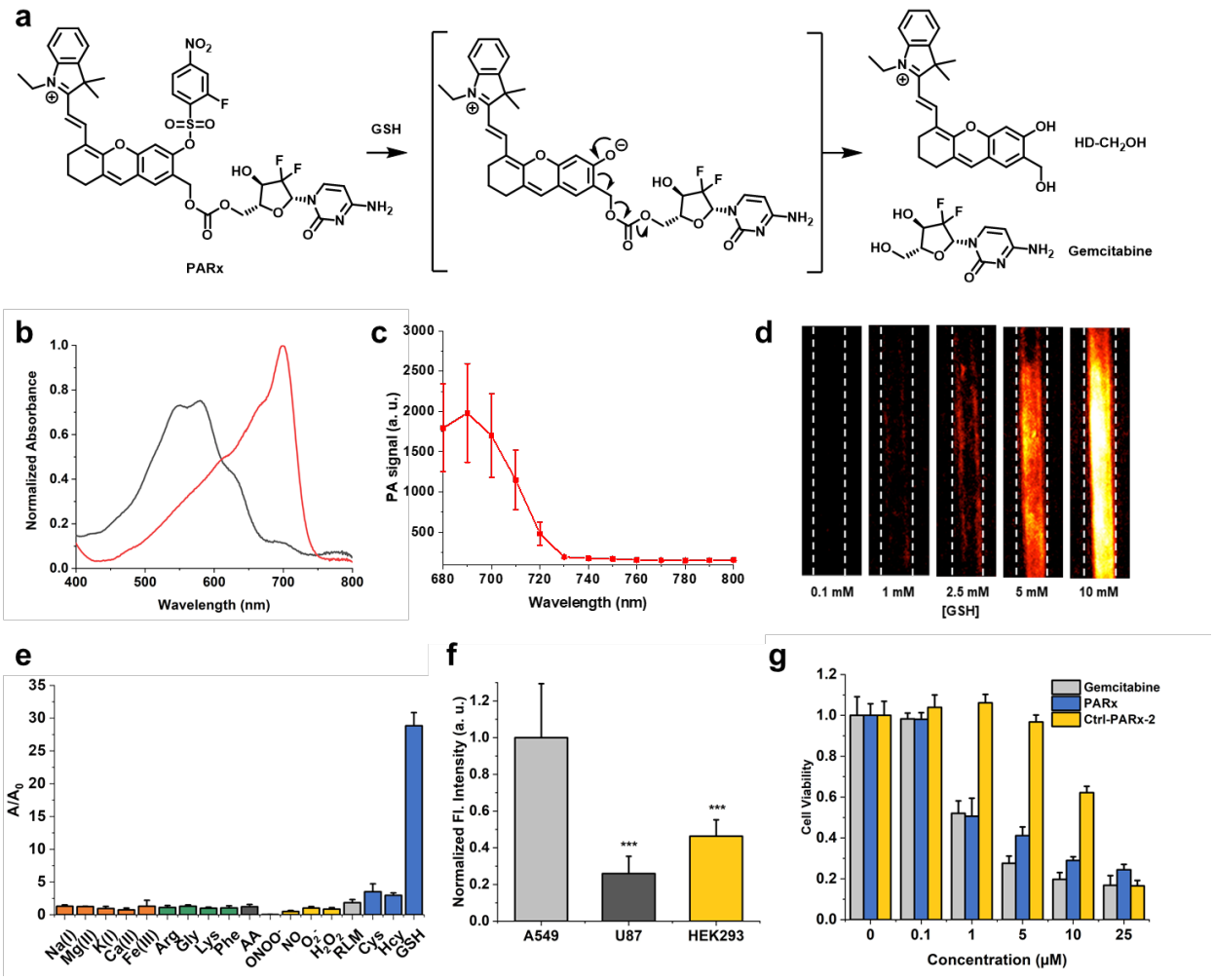

Figure 3. a) Reaction scheme of PARx with GSH to release HD-CH_2OH and Gemcitabine. b) Normalized absorbance profile of 5 μM PARx before (black line) and after (red line) treatment with 10 mM GSH at 37 °C for 1 h (pH 7.4, 70% PBS/MeCN). c) PA spectra of 50 μM turned over HD-CH_2OH dye in 70% PBS/MeCN. d) PA images of PARx in response to GSH. e) Reactivity of PARx with biologically relevant metals, amino acids, rat liver microsomes, ascorbic acid, RNS, ROS, and thiols after 1 h incubation at 37 °C. f) Normalized fluorescence intensity obtained from cell imaging A549, U87, and HEK293 cells with 5 μM PARx for 1 h at 37 ºC. Error bars = SD (n ≥ 3). g) Cell viability assay using various concentrations of Gemcitabine, PARx, and Ctrl-PARx-2 after 48 h incubation with A549 cells.

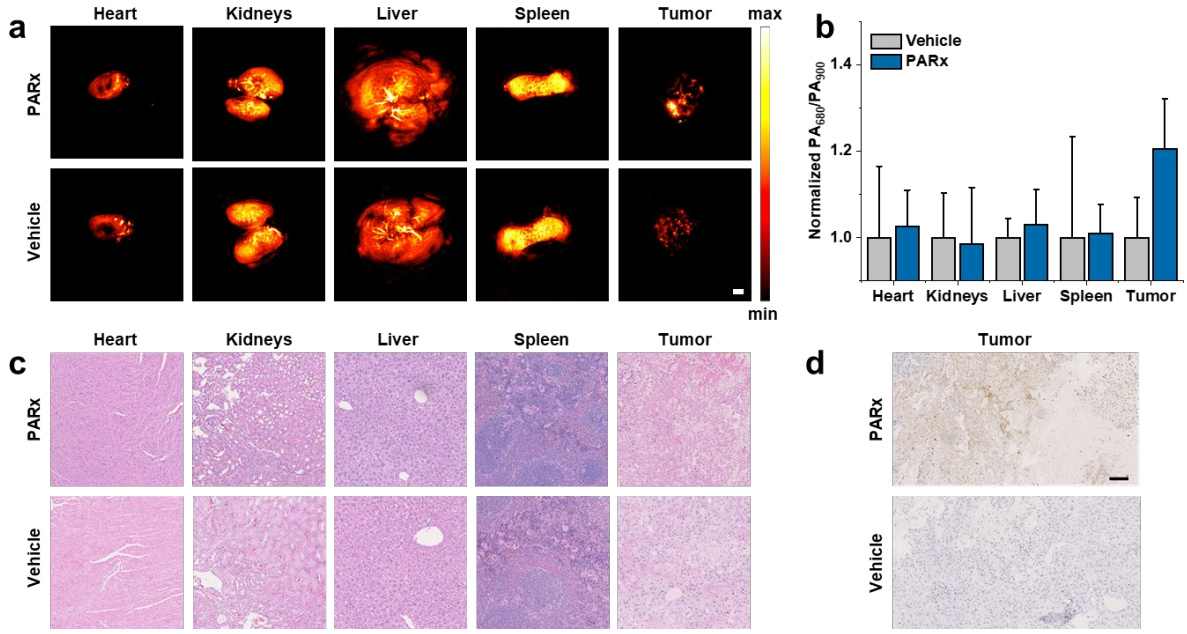

Figure 4. a) Representative *ex vivo* PA images of heart, kidneys, liver, spleen and tumor after systemic injection of PARx (400 μM, 10% DMSO/PBS, retro-orbital injection) or vehicle. Scale bar represents 2 mm. b) Normalized PA signal (relative to a reference probe-independent PA signal) after systemic injection of PARx or vehicle. Error bars = SD (*n* = 3). c) H&E staining of heart, kidney, liver, spleen, and tumor tissue from PARx-treated and untreated A549 xenografts. d) TUNEL staining of tumor tissue from PARx-treated and untreated A549 xenografts. Brown staining indicates apoptotic cell death. Scale bar represents 100 μm.

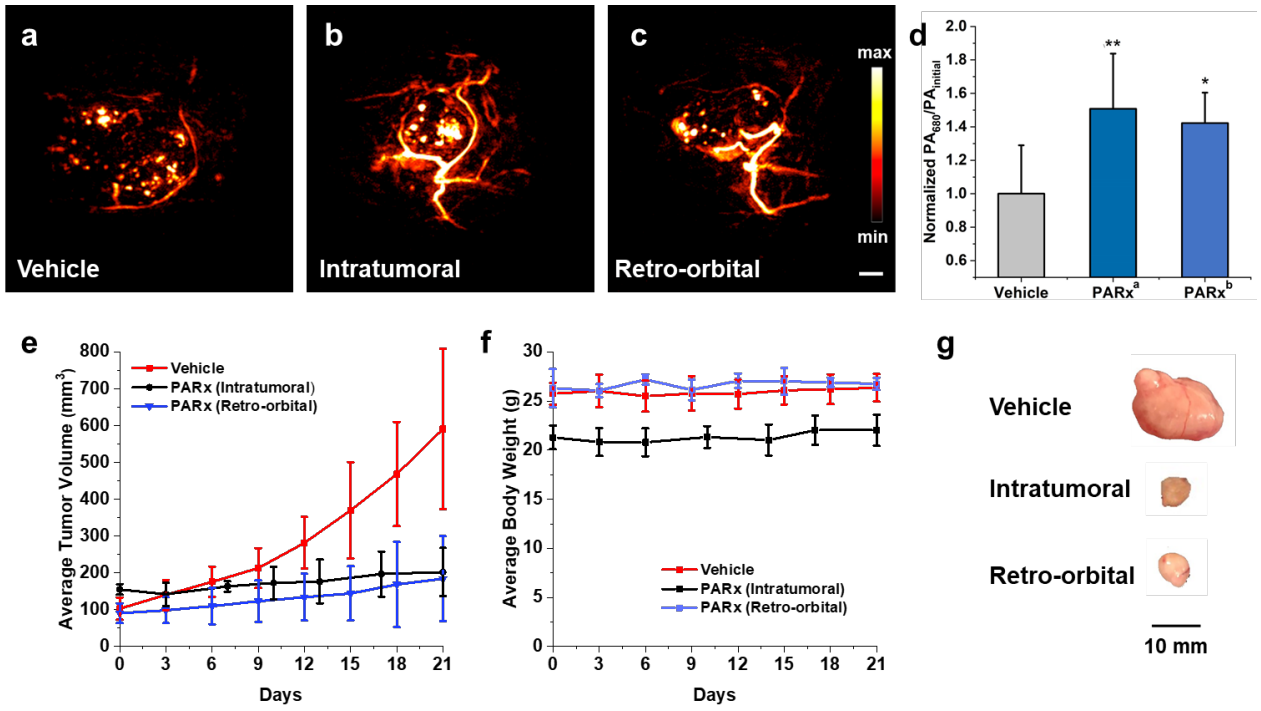

Figure 5. PA images of tumors after a) treatment with vehicle (10%DMSO/PBS), b) intratumoral injection of PARx (100 μM, 10% DMSO/PBS), or c) retro-orbital injection of PARx (400 μM, 10% DMSO/PBS). Scale bar represents 2 mm. d) Normalized PA signal after treatment with vehicle or PARx. a: intratumoral injection. b: retro-orbital injection. Error bars = SD (n = 3, tumor volume < 200 mm^3). e) Average tumor volume after treatment with vehicle, intratumoral, or retro-orbital injection of PARx over 21 days. f) Average body weight after treatment with vehicle, intratumoral, or retro-orbital injection of PARx over 21 days. g) Representative tumor photographs that were treated with vehicle, intratumoral, or retro-orbital injection of PARx. Statistical analysis was performed using Student's t-test, **: $p < 0.01$, *: $p < 0.05$.

References

1 Siegel, R. L., Miller, K. D. & Jemal, A. Cancer statistics, 2020. *CA: A Cancer Journal for Clinicians* **70**, 7-30, doi:10.3322/caac.21590 (2020).

2 Vogenberg, F. R., Isaacson Barash, C. & Pursel, M. Personalized medicine: part 1: evolution and development into theranostics. *P T* **35**, 560-576 (2010).

3 Dracopoli, N. C. & Boguski, M. S. The Evolution of Oncology Companion Diagnostics from Signal Transduction to Immuno-Oncology. *Trends in Pharmacological Sciences* **38**, 41-54, doi:10.1016/j.tips.2016.09.007 (2017).

4 Agarwal, A., Ressler, D. & Snyder, G. The current and future state of companion diagnostics. *Pharmgenomics Pers Med* **8**, 99-110, doi:10.2147/PGPM.S49493 (2015).

5 Chan, J., Dodani, S. C. & Chang, C. J. Reaction-based small-molecule fluorescent probes for chemoselective bioimaging. *Nature Chemistry* **4**, 973-984, doi:10.1038/nchem.1500 (2012).

6 Wang, L. V. & Hu, S. Photoacoustic Tomography: In Vivo Imaging from Organelles to Organs. *Science* **335**, 1458, doi:10.1126/science.1216210 (2012).

7 Heijblom, M. *et al.* Photoacoustic image patterns of breast carcinoma and comparisons with Magnetic Resonance Imaging and vascular stained histopathology. *Scientific Reports* **5**, 11778, doi:10.1038/srep11778 (2015).

8 Yang, M. *et al.* Photoacoustic/ultrasound dual imaging of human thyroid cancers: an initial clinical study. *Biomed. Opt. Express* **8**, 3449-3457, doi:10.1364/BOE.8.003449 (2017).

9 Jo, J. *et al.* A Functional Study of Human Inflammatory Arthritis Using Photoacoustic Imaging. *Scientific Reports* **7**, 15026, doi:10.1038/s41598-017-15147-5 (2017).

10 Liu, Y., Zhang, L., Li, S., Han, X. & Yuan, Z. Imaging molecular signatures for clinical detection of scleroderma in the hand by multispectral photoacoustic elastic tomography. *Journal of Biophotonics* **11**, e201700267, doi:10.1002/jbio.201700267 (2018).

11 Reinhardt, C. J. & Chan, J. Development of Photoacoustic Probes for in Vivo Molecular Imaging. *Biochemistry* **57**, 194-199, doi:10.1021/acs.biochem.7b00888 (2018).

12 Knox, H. J. & Chan, J. Acoustogenic Probes: A New Frontier in Photoacoustic Imaging. *Accounts of Chemical Research* **51**, 2897-2905, doi:10.1021/acs.accounts.8b00351 (2018).

13 Li, H., Zhang, P., Smaga, L. P., Hoffman, R. A. & Chan, J. Photoacoustic Probes for Ratiometric Imaging of Copper(II). *Journal of the American Chemical Society* **137**, 15628-15631, doi:10.1021/jacs.5b10504 (2015).

14 Mishra, A., Jiang, Y., Roberts, S., Ntziachristos, V. & Westmeyer, G. G. Near-Infrared Photoacoustic Imaging Probe Responsive to Calcium. *Analytical Chemistry* **88**, 10785-10789, doi:10.1021/acs.analchem.6b03039 (2016).

15 Roberts, S. *et al.* Calcium Sensor for Photoacoustic Imaging. *Journal of the American Chemical Society* **140**, 2718-2721, doi:10.1021/jacs.7b03064 (2018).

16 Wang, S. *et al.* Activatable Small-Molecule Photoacoustic Probes that Cross the Blood–Brain Barrier for Visualization of Copper(II) in Mice with Alzheimer's Disease. *Angewandte Chemie International Edition* **58**, 12415-12419, doi:10.1002/anie.201904047 (2019).

17 Knox, H. J. *et al.* A bioreducible N-oxide-based probe for photoacoustic imaging of hypoxia. *Nature Communications* **8**, 1794, doi:10.1038/s41467-017-01951-0 (2017).

18 Knox, H. J., Kim, T. W., Zhu, Z. & Chan, J. Photophysical Tuning of N-Oxide-Based Probes Enables Ratiometric Photoacoustic Imaging of Tumor Hypoxia. *ACS Chemical Biology* **13**, 1838-1843, doi:10.1021/acschembio.8b00099 (2018).

19 Chen, M. *et al.* Simultaneous photoacoustic imaging of intravascular and tissue oxygenation. *Opt. Lett.* **44**, 3773-3776, doi:10.1364/OL.44.003773 (2019).

20 Zhou, E. Y., Knox, H. J., Liu, C., Zhao, W. & Chan, J. A Conformationally Restricted Aza-BODIPY Platform for Stimulus-Responsive Probes with Enhanced Photoacoustic Properties. *Journal of the American Chemical Society* **141**, 17601-17609, doi:10.1021/jacs.9b06694 (2019).

21 Yin, L. *et al.* Quantitatively Visualizing Tumor-Related Protease Activity in Vivo Using a Ratiometric Photoacoustic Probe. *Journal of the American Chemical Society* **141**, 3265-3273, doi:10.1021/jacs.8b13628 (2019).

22 Levi, J. *et al.* Design, Synthesis, and Imaging of an Activatable Photoacoustic Probe. *Journal of the American Chemical Society* **132**, 11264-11269, doi:10.1021/ja104000a (2010).

23 Reinhardt, C. J., Zhou, E. Y., Jorgensen, M. D., Partipilo, G. & Chan, J. A Ratiometric Acoustogenic Probe for in Vivo Imaging of Endogenous Nitric Oxide. *Journal of the American Chemical Society* **140**, 1011-1018, doi:10.1021/jacs.7b10783 (2018).

24 Reinhardt, C. J., Xu, R. & Chan, J. Nitric oxide imaging in cancer enabled by steric relaxation of a photoacoustic probe platform. *Chemical Science* **11**, 1587-1592, doi:10.1039/C9SC05600A (2020).

25 Chen, Z. *et al.* An Optical/Photoacoustic Dual-Modality Probe: Ratiometric in/ex Vivo Imaging for Stimulated H2S Upregulation in Mice. *Journal of the American Chemical Society* **141**, 17973-17977, doi:10.1021/jacs.9b09181 (2019).

26 Yuan, L. *et al.* A Unique Approach to Development of Near-Infrared Fluorescent Sensors for in Vivo Imaging. *Journal of the American Chemical Society* **134**, 13510-13523, doi:10.1021/ja305802v (2012).

27 Forman, H. J., Zhang, H. & Rinna, A. Glutathione: Overview of its protective roles, measurement, and biosynthesis. *Molecular Aspects of Medicine* **30**, 1-12, doi:https://doi.org/10.1016/j.mam.2008.08.006 (2009).

28 Balendiran, G. K., Dabur, R. & Fraser, D. The role of glutathione in cancer. *Cell Biochemistry and Function* **22**, 343-352, doi:10.1002/cbf.1149 (2004).

29 Gamcsik, M. P., Kasibhatla, M. S., Teeter, S. D. & Colvin, O. M. Glutathione levels in human tumors. *Biomarkers* **17**, 671-691, doi:10.3109/1354750X.2012.715672 (2012).

30 Russo, A., DeGraff, W., Friedman, N. & Mitchell, J. B. Selective Modulation of Glutathione Levels in Human Normal versus Tumor Cells and Subsequent Differential Response to Chemotherapy Drugs. *Cancer Research* **46**, 2845 (1986).

31 Giustarini, D. *et al.* Glutathione, glutathione disulfide, and S-glutathionylated proteins in cell cultures. *Free Radical Biology and Medicine* **89**, 972-981, doi:https://doi.org/10.1016/j.freeradbiomed.2015.10.410 (2015).

32 Lee, M. H. *et al.* Disulfide-Cleavage-Triggered Chemosensors and Their Biological Applications. *Chemical Reviews* **113**, 5071-5109, doi:10.1021/cr300358b (2013).

33 Maeda, H. *et al.* 2,4-Dinitrobenzenesulfonyl Fluoresceins as Fluorescent Alternatives to Ellman's Reagent in Thiol-Quantification Enzyme Assays. *Angewandte Chemie International Edition* **44**, 2922-2925, doi:10.1002/anie.200500114 (2005).

34 Zhang, J. *et al.* Synthesis and Characterization of a Series of Highly Fluorogenic Substrates for Glutathione Transferases, a General Strategy. *Journal of the American Chemical Society* **133**, 14109-14119, doi:10.1021/ja205500y (2011).

35 Shibata, A. *et al.* Fluorogenic probes using 4-substituted-2-nitrobenzenesulfonyl derivatives as caging groups for the analysis of human glutathione transferase catalyzed reactions. *Analyst* **138**, 7326-7330, doi:10.1039/C3AN01339A (2013).

36 van Iersel, M. L. P. S. *et al.* Inhibition of glutathione S-transferase activity in human melanoma cells by α,β-unsaturated carbonyl derivatives. Effects of acrolein, cinnamaldehyde, citral, crotonaldehyde, curcumin, ethacrynic acid, and trans-2-hexenal. *Chemico-Biological Interactions* **102**, 117-132, doi:https://doi.org/10.1016/S0009-2797(96)03739-8 (1996).

37 Rahman, I., Kode, A. & Biswas, S. K. Assay for quantitative determination of glutathione and glutathione disulfide levels using enzymatic recycling method. *Nature Protocols* **1**, 3159-3165, doi:10.1038/nprot.2006.378 (2006).

38 Manegold, C. Gemcitabine (Gemzar®) in non-small cell lung cancer. *Expert Review of Anticancer Therapy* **4**, 345-360, doi:10.1586/14737140.4.3.345 (2004).

39 Hayashi, H., Kurata, T. & Nakagawa, K. Gemcitabine: Efficacy in the Treatment of Advanced Stage Nonsquamous Non-Small Cell Lung Cancer. *Clinical Medicine Insights: Oncology* **5**, CMO.S6252, doi:10.4137/CMO.S6252 (2011).

40 Toschi, L., Finocchiaro, G., Bartolini, S., Gioia, V. & Cappuzzo, F. Role of gemcitabine in cancer therapy. *Future Oncology* **1**, 7-17, doi:10.1517/14796694.1.1.7 (2005).

41 He, M., Xuehong, C. & Yepeng, L. Small Molecular Gemcitabine Prodrugs for Cancer Therapy. *Current Medicinal Chemistry* **26**, 1-20, doi:http://dx.doi.org/10.2174/0929867326666190816230650 (2019).

42 Ullman-Cullere, M. H. & Foltz, C. J. Body condition scoring: a rapid and accurate method for assessing health status in mice. *Lab Anim Sci* **49**, 319-323 (1999).

43 Cook, J. A., Iype, S. N. & Mitchell, J. B. Differential Specificity of Monochlorobimane for Isozymes of Human and Rodent Glutathione S-Transferases. *Cancer Research* **51**, 1606 (1991).